High-accuracy calculations of sixteen collision integrals for Lennard-Jones (12−6) gases and their interpolation to…

2 authors:

Sun Ung Kim
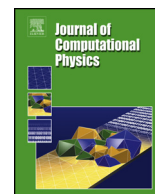Bosch Research and Technology Center Nort…
13 PUBLICATIONS **49** CITATIONS

Charles W. Monroe
University of Oxford
61 PUBLICATIONS **1,083** CITATIONS

High-accuracy calculations of sixteen collision integrals for Lennard-Jones (12–6) gases and their interpolation to parameterize neon, argon, and krypton

Sun Ung Kim [a], Charles W. Monroe [b],*

[a] *Department of Mechanical Engineering, University of Michigan, Ann Arbor, MI 48109, USA*
[b] *Department of Chemical Engineering, University of Michigan, Ann Arbor, MI 48109, USA*

A R T I C L E   I N F O

A B S T R A C T

The inverse problem of parameterizing intermolecular potentials given macroscopic transport and thermodynamic data is addressed. Procedures are developed to create arbitrary-precision algorithms for transport collision integrals, using the Lennard-Jones (12–6) potential as an example. Interpolation formulas are produced that compute these collision integrals to four-digit accuracy over the reduced-temperature range $0.3 \leq T^* \leq 400$, allowing very fast computation. Lennard-Jones parameters for neon, argon, and krypton are determined by simultaneously fitting the observed temperature dependences of their viscosities and second virial coefficients—one of the first times that a thermodynamic and a dynamic property have been used simultaneously for Lennard-Jones parameterization. In addition to matching viscosities and second virial coefficients within the bounds of experimental error, the determined Lennard-Jones parameters are also found to predict the thermal conductivity and self-diffusion coefficient accurately, supporting the value of the Lennard-Jones (12–6) potential for noble-gas transport-property correlation.

1. Introduction

Accurate transport properties are crucial for the simulation of processes involving continuum-scale momentum, heat, or mass transfer. Gas viscosities, thermal conductivities, and diffusivities, for example, are needed in the design of chemical reactors, and also play an important role in atmospheric chemistry, combustion science, and aerothermodynamics [1,2]. Direct measurements of all the properties of a gas over a wide temperature range are usually impractical, so there is a need for reliable methods of property estimation [2].

Kinetic theory, as implemented through the analysis of Boltzmann's gas equation [3], provides a well-established method to calculate macroscopic transport coefficients. Conventional wisdom has it that the theory can predict temperature-dependent transport properties of dilute nonpolar gases with fair agreement [4]. This paper provides a method to work backwards from experimental data to extract potential parameters. For neon, argon, and krypton, the kinetic-theory predictions are found to fall within the bounds of intrinsic measurement error.

Gressman and Strain's work on stable solutions to the Boltzmann equation [5] emphasizes that the approach developed by Chapman and Enskog a century ago [6–8] is a mathematically sound way to compute continuum properties.

---

* Corresponding author.
  E-mail addresses: sunung@umich.edu (S.U. Kim), cwmonroe@umich.edu (C.W. Monroe).

Chapman–Enskog theory uses a perturbation analysis of Boltzmann's equation to express transport coefficients as algebraic functions of reduced collision integrals $\Omega^{(l,s)\star}$ [9,10].

For a pure, dilute gas, collision integrals depend only on a reduced temperature $T^* = k_B T/\epsilon$, where k_B is Boltzmann's constant, T the absolute temperature, and ϵ a characteristic two-particle interaction energy. Thus $\Omega^{(l,s)\star}$ values are amenable to tabulation—in principle. Several well-known difficulties impede numerical analysis: divergences, discontinuities, and rapid oscillations occur in several functions from which collision integrals derive [1]. Because of the high computational cost and analytical complexity of their calculation, collision integrals are usually retrieved from tables, rather than being computed on the fly. Yet procedures for interpolation between temperatures remain poorly established.

In the discussion below, analysis of two-particle interaction trajectories is used to inform accurate collision-integral computation. By leveraging knowledge about trajectory shapes, collision cross-sections can be computed with unprecedented precision. This approach is quite general; the Lennard-Jones (LJ) potential model is used below as an example.

A great deal of kinetic-theory research in the past three or four decades has focused on the development and computational implementation of novel potential functions for noble gases, with the aims of better describing condensed phases, accounting for spectroscopic observations in more detail, and modeling covalent dimerization phenomena [11,12]. For rarefied gases, *ab initio* potentials have been developed and applied, providing the highest level of fundamental physical detail [13,14]. Despite its limitations, the present work focuses on the classical LJ model because of its popularity for property estimation in engineering applications. The LJ potential also has a simple shape and involves only two parameters, making it straightforward to illustrate how interaction trajectories can be useful and how parameterization based on macroscopic properties can be implemented.

Akhmatskaya and Pozhar have demonstrated [15] that many well-known tables and interpolation formulas describing LJ interactions [9,16,17] summarize inaccurate calculations. Neufeld, Janzen, and Aziz (NJA) produced some of the most commonly cited interpolation formulas for LJ (12–6) collision integrals. The sixteen formulas they provided allow viscosity, thermal conductivity, self-diffusion coefficient, and thermal diffusivity to be computed up to third order for $0.3 \le T^* \le 100$ [17,18]. A database computed with O'Hara and Smith's algorithm [19] underpins the NJA formulas, which are precise to one or two digits at most. Below we develop arbitrary-precision algorithms for collision-integral computation, and provide empirical interpolations for LJ (12–6) gases accurate to at least four significant digits for $0.3 \le T^* \le 400$.

To illustrate their utility, the interpolation formulas are deployed to solve the inverse problem of potential parameterization. Three noble gases are analyzed. Previous apparent disagreements between LJ theory and experiments are resolved by leveraging fast, precise collision-integral calculation. For dilute neon, argon, and krypton, the LJ potential simultaneously matches viscosity, self-diffusion coefficient, thermal conductivity, and second virial coefficient within experimental error, from their boiling points up to extremely high temperatures. Thus, although it may be deficient in other aspects for these gases, the LJ model suffices to predict most thermodynamic and transport properties relevant to computational-fluid-dynamics simulations.

2. Collision-integral interpolation

Since it provides a basis for putting this work to broader practical use, we first present empirical interpolation formulas for reduced LJ (12–6) collision integrals. Fig. 1 demonstrates that the functionality

$$\Omega^{(l,s)\star} = A^{(l,s)} + \sum_{k=1}^{6}\left[\frac{B_k^{(l,s)}}{(T^*)^k} + C_k^{(l,s)}\left(\ln T^*\right)^k\right] \tag{1}$$
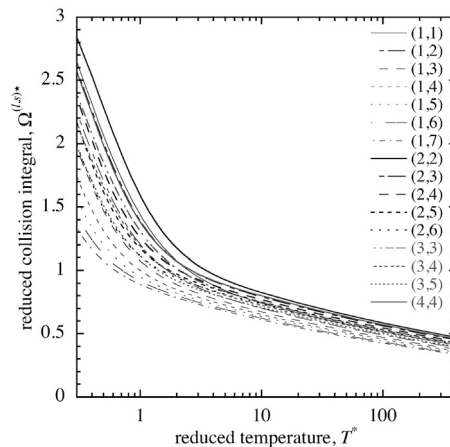

Fig. 1. Reduced collision integrals for Lennard-Jones (12–6) gases, computed using the methods developed in Section 3.

Table 1
Coefficients for Eq. (1), which predicts collision integrals within 0.007% in the range $0.3 \leq T^* \leq 400$.

| (l, s)	$A^{(l,s)}$	$B_1^{(l,s)}$	$C_1^{(l,s)}$	$B_2^{(l,s)}$	$C_2^{(l,s)} \times 10$	$B_3^{(l,s)} \times 10$	$C_3^{(l,s)} \times 10$
(1, 1)	−1.1036729	2.6431984	1.6690746	0.0060432255	−6.9145890	−1.5158773	1.5502132
(1, 2)	1.3555554	−0.44668594	−0.47499422	0.42734391	1.4482036	−1.6036459	−0.32158368
(1, 3)	1.0677115	−0.13945390	−0.25258689	0.17696362	0.59709197	−0.26252211	−0.13332695
(1, 4)	0.80959899	0.12938170	−0.045055948	0.059760309	−0.22642753	0.071109469	0.056672308
(1, 5)	0.74128322	0.17788850	0.0013668724	0.027398438	−0.41730962	0.076254248	0.10378923
(1, 6)	0.80998324	0.073071217	−0.071180849	0.034607908	−0.12738119	−0.011457199	0.038582834
(1, 7)	0.81808091	0.044232851	−0.089417548	0.029750283	−0.051856424	−0.022011682	0.021882143
(2, 2)	−0.92032979	2.3508044	1.6330213	0.50110649	−6.9795156	−4.7193769	1.6096572
(2, 3)	2.5955799	−1.8569443	−1.4586197	0.96985775	5.2947262	−3.9888526	−1.1946363
(2, 4)	1.6042745	−0.67406115	−0.62774499	0.42671907	2.0700644	−1.0177069	−0.47601690
(2, 5)	0.82064641	0.23195128	0.039184885	0.12233793	−0.57316906	0.13891578	0.12794497
(2, 6)	0.79413652	0.23766123	0.050470266	0.077125802	−0.62621672	0.13060901	0.14326724
(3, 3)	1.2630491	−0.36104243	−0.33227158	0.68116214	0.79723851	−3.6401583	−0.15470355
(3, 4)	2.2114636	−1.4743107	−1.1942554	0.64918549	4.3000688	−2.4075196	−0.97525871
(3, 5)	1.5049809	−0.64335529	−0.60014514	0.3261704	1.9764859	−0.82126072	−0.45212434
(4, 4)	2.6222393	−1.9158462	−1.4676253	1.0166380	5.3048161	−4.3355278	−1.1909781

(l, s)	$B_4^{(l,s)} \times 10$	$C_4^{(l,s)} \times 10^2$	$B_5^{(l,s)} \times 10^2$	$C_5^{(l,s)} \times 10^3$	$B_6^{(l,s)} \times 10^3$	$C_6^{(l,s)} \times 10^4$
(1, 1)	0.54237938	−2.0642189	−0.90468682	1.5402077	0.61742007	−0.49729535
(1, 2)	0.31461648	0.44357933	−0.32587575	−0.34138118	0.13860257	0.11259742
(1, 3)	−0.043814141	0.19619285	0.16752100	−0.16063076	−0.14382801	0.055804557
(1, 4)	−0.063851124	−0.065708760	0.10498938	0.040733113	−0.058149257	−0.010820157
(1, 5)	−0.031650182	−0.13492954	0.032786518	0.096963599	−0.0092890016	−0.030307552
(1, 6)	0.0028198596	−0.047060425	−0.020060540	0.030466929	0.021446483	−0.0085305576
(1, 7)	0.0063264120	−0.024874471	−0.017555530	0.013745859	0.014255704	−0.0030285365
(2, 2)	1.5806367	−2.2109440	−2.6367184	1.7031434	1.8120118	−0.56699986
(2, 3)	0.90063692	1.6264589	−1.0918991	−1.2354315	0.56646797	0.40366357
(2, 4)	0.0061857136	0.67153792	0.31225358	−0.52706167	−0.35206051	0.17705708
(2, 5)	−0.20903423	−0.15336449	0.46715462	0.10241454	−0.35204303	−0.029975563
(2, 6)	−0.10982362	−0.17806541	0.18034505	0.12353365	−0.095982571	−0.037501381
(3, 3)	1.0500196	0.18686705	−1.6400134	−0.12179945	1.0880886	0.032594587
(3, 4)	0.51820149	1.3399366	−0.60565396	−1.0283777	0.29812326	0.33956674
(3, 5)	0.059682011	0.63650284	0.10269488	−0.49991689	−0.15957252	0.16833944
(4, 4)	1.0496591	1.6123847	−1.3951104	−1.2174905	0.80048534	0.39545100

Table 2
Average and maximum deviations from tables accurate to seven digits past the decimal for the interpolation formulas in Eq. (1).

(l, s)	Average deviation (%)	Maximum deviation (%)
(1, 1)	0.00099	0.0051 at $T^* = 300$
(1, 2)	0.00041	0.0025 at $T^* = 0.55$
(1, 3)	0.00031	0.0011 at $T^* = 400$
(1, 4)	0.00022	0.00093 at $T^* = 0.8$
(1, 5)	0.00020	0.00095 at $T^* = 0.7$
(1, 6)	0.00025	0.00099 at $T^* = 0.7$
(1, 7)	0.00023	0.00099 at $T^* = 0.6$
(2, 2)	0.0011	0.0071 at $T^* = 300$
(2, 3)	0.00063	0.0030 at $T^* = 200$
(2, 4)	0.00035	0.0018 at $T^* = 200$
(2, 5)	0.00022	0.0012 at $T^* = 0.5$
(2, 6)	0.00024	0.00085 at $T^* = 0.85$
(3, 3)	0.00037	0.0021 at $T^* = 0.45$
(3, 4)	0.00054	0.0033 at $T^* = 200$
(3, 5)	0.00038	0.0020 at $T^* = 200$
(4, 4)	0.00041	0.0029 at $T^* = 200$

reasonably approximates the first sixteen most useful collision integrals, which all decrease with rising T^* according to the form of the summand. Values of the coefficients in Eq. (1) are given in Table 1 for the sixteen combinations of l and s shown in Fig. 1. Coefficients were determined by applying an optimization procedure based on the method of least squares [20] to a database of collision-integral tables, produced using the arbitrary-precision procedures described in Section 3. Table 2 summarizes the error of Eq. (1) relative to the high-precision tables on which it is based. For $0.3 \leq T^* \leq 400$, the average error is always less than 0.0011% and the maximum error less than 0.0069%; Eq. (1) yields collision integrals accurate to at least four significant digits throughout this temperature range.
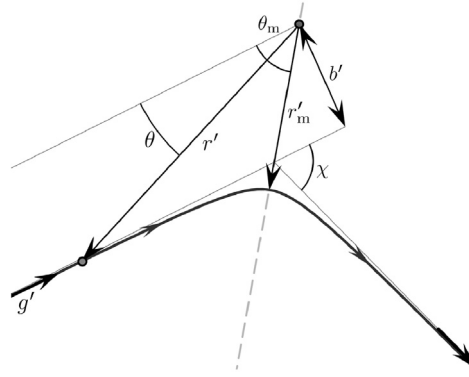
Fig. 2. Schematic of a binary encounter, characterized by the trajectory $r'(\theta)$. The initial relative particle speed g' and impact parameter b' determine the deflection angle χ.

Unlike the NJA fit, Eq. (1) has a series form wherein coefficients generally decrease in magnitude as their order rises. One might think that adding terms to the sum would reduce deviations from the data tables on which it is based, but use of more than six terms in the series was found to increase truncation error overall when the coefficients were truncated after their eighth significant digit (as in Table 1). Note also that the NJA parameterization was designed for accuracy within the range $0.3 \leq T^* \leq 100$; in contrast, Eq. (1) is designed for accuracy up to reduced temperatures of 400.

3. Precise collision-integral calculation

3.1. Description of encounters

Chapman–Enskog theory hinges on the detailed description of individual two-particle encounters, which are described by momentum balances. Several researchers have embedded quantum effects into kinetic theory [21–23], but quantum corrections tend to contribute negligibly to collision integrals [22]. Classical physics is employed here.

A representative classical binary encounter is sketched schematically in Fig. 2. Encounters are treated in a polar coordinate system (r', θ) centered on one particle (which we call the 'incident particle'), in the plane established by the two particle velocities, with $\theta = 0$ aligned parallel to the direction of the relative velocity of the other particle (called the 'incoming particle'). (This perspective is equivalent to the center-of-mass coordinates used by Grad [10,24]; here we follow the particle-center convention used by Chapman and Cowling [7,8] and Hirschfelder et al. [9,25–27].) Collision trajectories $r'(\theta)$ depend on the initial relative particle speed g', as well as the impact parameter b', which represents the distance of closest approach that would be achieved if the two particles did not exert any forces on each other during the encounter.

The energetics of particle interactions depend on a pair potential ϕ', which always has some repulsive character, and usually also has some attractive character. For a pair of similar particles, the trajectory during an encounter conserves angular momentum and energy, according to

$$mb'g' = mr'^2 \frac{d\theta}{dt}, \tag{2}$$

$$\frac{1}{2}mg'^2 = \frac{1}{2}m\left[\left(\frac{dr'}{dt}\right)^2 + r'^2\left(\frac{d\theta}{dt}\right)^2\right] + \phi'(r'), \tag{3}$$

where t is time and m is the particle mass. The potential thus establishes how g' and b' determine the angle χ by which the relative velocity deflects during an encounter.

The character of an encounter trajectory ultimately depends on the functionality of the pair potential. Chapman and Cowling [7,8] used a hard-sphere potential to determine coefficients of viscosity, thermal conductivity, and self-diffusion. The accuracy of these transport coefficients was limited by the failure to account for interparticle attraction. Diffusivities computed for hard-sphere gases generally exceed experimental values by 10–15% at moderate temperatures [28].

Kihara and Kotani [29,30], Hirschfelder et al. [9,25–27], and Rowlinson [31] concurrently reported transport coefficients based on the LJ (12–6) interaction potential [32,33]

$$\phi'(r') = 4\epsilon\left[\left(\frac{\sigma}{r'}\right)^{12} - \left(\frac{\sigma}{r'}\right)^6\right]. \tag{4}$$

Here σ is the distance at which the potential crosses zero (it reaches a minimum at $r'/\sigma = \sqrt[6]{2} \approx 1.12$), and the characteristic energy ϵ quantifies the depth of the potential well. The term 'LJ parameters' will be used here to refer to the characteristic temperature ϵ/k_B and characteristic distance σ. Unlike the hard-sphere model, the LJ (12–6) potential accounts for interparticle attraction, whose sixth-order decay is suggested by quantum-mechanical analysis of non-polar,

neutral atoms with spherically symmetric electron shells [34–36]; mathematical convenience is afforded by choosing a twelfth-order repulsive term [9]. When potentials involve both attraction and repulsion, the evaluations of collision integrals are complicated, because they must account for orbiting and spiraling trajectories [1], which will be a key focus here.

To determine the trajectory traversed during a binary encounter it is standard to obtain a time-independent expression of the angle θ by eliminating dt between Eqs. (2) and (3); after substituting ϕ' from Eq. (4), one obtains

$$\theta(y; b, g) = \int_0^y \frac{bg\,dy}{\sqrt{P(y; b, g)}}, \tag{5}$$

where the polynomial P is defined as

$$P(y; b, g) = g^2\left(1 - b^2 y^2\right) + 4\left(y^6 - y^{12}\right). \tag{6}$$

Eqs. (5) and (6) introduce dimensionless variables

$$b = \frac{b'}{\sigma}, \qquad g^2 = \frac{\frac{1}{2}m(g')^2}{\epsilon}, \qquad \phi = \frac{\phi'}{\epsilon}, \quad \text{and} \quad y = \frac{\sigma}{r'}. \tag{7}$$

A dimensionless inverse radius y changes the integration domain in Eq. (5) from open, $r' \in [r', \infty)$, to closed, $y \in [0, y]$.

The dimensionless inverse distance of closest approach, y_m, is the smallest positive root of the polynomial P,

$$y_m(b, g) = \min\left\{y_m^i : y_m^i \in \Re^+, P\left(y_m^i; b, g\right) = 0\right\}. \tag{8}$$

For a given binary encounter, the incoming trajectory can be drawn with Eq. (5); the outgoing trajectory can be found by reflection about a radial line inclined at the closest-approach angle $\theta_m = \theta(y_m; b, g)$.

Reduced collision integrals $\Omega^{(l,s)\star}$ result from a threefold integration: one over all inverse trajectory radii, the closed domain $y \in [0, y_m]$; one over all impact parameters, the semi-infinite domain $b \in [0, \infty)$; and one over all relative speeds, $g \in [0, \infty)$. The sequence of integrals used to compute $\Omega^{(l,s)\star}$ is [9,25–27]

$$\chi(b, g) = \pi - 2\theta_m = \pi - 2bg \int_0^{y_m} \frac{dy}{\sqrt{P(y; b, g)}}; \tag{9}$$

$$Q^{(l)\star}(g) = \frac{2}{1 - \frac{1}{2}\frac{1+(-1)^l}{1+l}} \int_0^\infty \left(1 - \cos^l \chi\right)b\,db; \tag{10}$$

$$\Omega^{(l,s)\star} = \frac{2}{(s+1)!\,T^{*s+2}} \int_0^\infty e^{-g^2/T^*} g^{2s+3} Q^{(l)\star}\,dg. \tag{11}$$

These include the deflection angle χ (cf. Fig. 2) and introduce the reduced collision cross-section $Q^{(l)\star}$. (Quantities with a superscript $\star$ are scaled by the corresponding functions obtained with a hard-sphere potential.)

The hyper-elliptic integral that arises in Eq. (9) for LJ (12–6) particles cannot be solved analytically. While computing collision integrals numerically, y_m, χ, $Q^{(l)\star}$, and $\Omega^{(l,s)\star}$ must be calculated within strict accuracy limits. Singularities, discontinuities, and oscillations of the functions involved impede high-precision calculations [1].

3.2. Distance of closest approach

The reciprocal closest approach distance y_m (cf. Eq. (8)) must be calculated first, because it sets the upper bound of integration in Eq. (9). At this stage it is important to assess whether P (cf. Eq. (6)) affords multiple real positive roots. When interaction potentials have both attractive and repulsive character, two particles can spiral around each other or even fall into orbit (following 'looping' trajectories), rather than undergoing a simple collision. Orbits correspond to parameter combinations that yield minimal real positive roots of P with multiplicity higher than 1.

Akhmatskaya and Pozhar found conditions that lead to orbits [15] using the characteristic of double roots

$$P\left(y_m^i; b, g\right) = \left.\frac{dP}{dy}\right|_{(y_m^i; b, g)} = 0. \tag{12}$$

One thus finds that y_m^i is a double root of P when

$$y_m^i = \sqrt[6]{\frac{1}{5} \pm \frac{1}{5}\sqrt{1 - \frac{5}{4}g^2}}. \tag{13}$$

Insertion of Eq. (13) into Eq. (6) determines a relationship between b and g that, when satisfied, shows that an encounter results in an orbit. Only the smaller root in Eq. (13) yields orbiting trajectories; the larger does not satisfy Eq. (8).
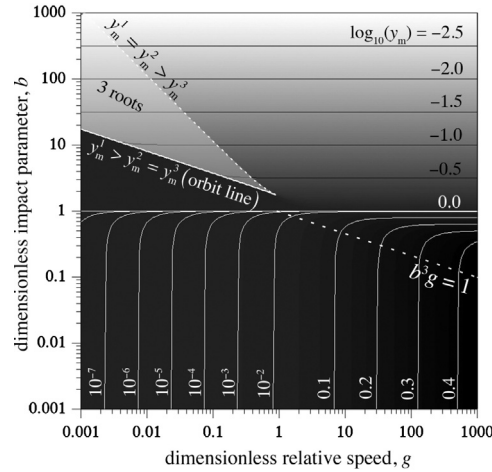
Fig. 3. Contour plot of the inverse closest-approach distance y_m with respect to b and g for Lennard-Jones (12–6) particles. The polynomial P of Eq. (6) affords either three real positive roots or just one in this domain. On the 'orbit line' b and g combine to make the deflection angle χ diverge.

One might ask whether combinations of b and g that satisfy Akhmatskaya and Pozhar's conditions are the *only* orbiting trajectories in the domains of b and g. Uniqueness can be proved by enumerating the real positive roots afforded by the polynomial P. Hostetter's modification to the Routh–Hurwitz test [37,38] allows the values of a polynomial's coefficients to be used to count how many real, positive roots it affords. The Hostetter–Routh–Hurwitz test shows P has three real positive roots when $g \leq 2/\sqrt{5}$,

$$\frac{2\sqrt{3}}{g\sqrt[3]{5}}\sqrt[3]{1 - \sqrt{1 - \tfrac{5}{4}g^2}}\sqrt{\tfrac{3}{5} + \tfrac{2}{5}\sqrt{1 - \tfrac{5}{4}g^2}} \leq b, \quad \text{and} \quad b \leq \frac{2\sqrt{3}}{g\sqrt[3]{5}}\sqrt[3]{1 + \sqrt{1 - \tfrac{5}{4}g^2}}\sqrt{\tfrac{3}{5} - \tfrac{2}{5}\sqrt{1 - \tfrac{5}{4}g^2}}. \tag{14}$$

Otherwise, P possesses a single real positive root.

Fig. 3 summarizes characteristics of the polynomial P and values of its least root y_m. Two lines in the figure delineate the boundaries of the domains of b and g where P affords repeat positive roots. On the upper ($y_m^1 = y_m^2 > y_m^3$) and the lower ($y_m^1 > y_m^2 = y_m^3$) lines, one of the three roots has multiplicity 2; there is a triple root at the point $(g, b) = (2/\sqrt{5}, 3/\sqrt[3]{5})$. The upper double-root line in Fig. 3 has no physical significance because if the double root is larger than the single root, a trajectory will never traverse its position. The lower double-root line corresponds to a situation where two particles fall into orbit during an encounter. Because of this characteristic, it is labeled as the 'orbit line' in Fig. 3. The orbit line is a function of $g \leq 2/\sqrt{5}$; orbiting b values in that domain are given by

$$b_o(g) = \frac{2\sqrt{3}}{g\sqrt[3]{5}}\sqrt[3]{1 - \sqrt{1 - \tfrac{5}{4}g^2}}\sqrt{\tfrac{3}{5} + \tfrac{2}{5}\sqrt{1 - \tfrac{5}{4}g^2}}. \tag{15}$$

Newton's method [39] was used in combination with Horner's scheme for synthetic division [40] to establish the positions of the real roots of P with high accuracy. The asymptotic behavior of y_m helps provide a clue toward useful initial guesses for the algorithm. The shapes of the y_m contours in Fig. 3 change around a hypothetical line $b^3 g = 1$. Asymptotic analyses show that the following relations are reliable initial guesses for roots:

$$y_m \approx \begin{cases} 1 & \text{if } g < \frac{2}{\sqrt{5}} \text{ and } b < b_o, \\ \sqrt[6]{\frac{1}{2} + \frac{1}{2}\sqrt{1 + g^2}} & \text{if } g \geq \frac{2}{\sqrt{5}} \text{ and } b^3 g \ll 1, \\ \frac{1}{b} & \text{if } b > b_o \text{ or } b^3 g \gg 1. \end{cases} \tag{16}$$

When $b^3 g \approx 1$, the last two guesses yield similar results. In this work $1/b$ was used when $b > b_o$ or $b^3 g \geq 1$.

Newton's method reliably finds the first root of P. In the 3-root region, P can be reduced in order by synthetic division, Newton's method can be applied to locate the second root, and a sequential division can be performed to find the third. Truncation errors can be mitigated by using these results as guesses for roots with the original polynomial P.

High-precision y_m values are essential; their accuracy limits all further calculations. To verify accuracy, Eqs. (6) and (8) were combined, yielding

$$\tilde{b}(g, y_m) = \frac{2y_m^2}{g}\sqrt{\frac{g^2}{4y_m^6} + 1 - y_m^6}. \tag{17}$$
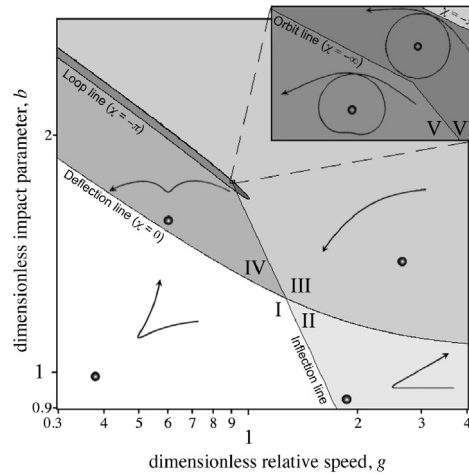
Fig. 4. Map showing how trajectory shapes depend on the impact parameter and relative speed for binary Lennard-Jones (12–6) interactions. Six different trajectory types, drawn using Eq. (5), are represented. An inset shows behavior in the region bounded by the loop line, where spiraling trajectories occur. Orbits ($\chi \to -\infty$), undeflected trajectories ($\chi = 0$) and head-on collisions ($b = 0$, $\chi = \pi$) have no statistical weight in the ensemble and are not depicted.

Here $\tilde{b}$ is equivalent to b; their difference tracks the accuracy of y_{m}. (When y_{m} nears 1, a new variable $x_{\mathrm{m}} = y_{\mathrm{m}} - 1$ can be introduced to avoid truncation error.) Eq. (17) confirmed that y_{m} values were accurate to 14 significant digits.

3.3. Deflection angle

Once closest-approach distances y_{m} are known, the task of evaluating the deflection angle χ presents itself. Since P always has at least one real positive root, the integrand in Eq. (9) always has a singularity at the upper bound of integration. Roots at the upper bound correspond to poles in the integrand of order 1/2, 1, or 3/2.

Singularities of order 1/2 at $y = y_{\mathrm{m}}$ in the integrand can be removed by a change of integration variable. First, relying on the fact that P is even, factor it to

$$P(y; b, g) = \frac{(y_{\mathrm{m}} - y)(y_{\mathrm{m}} + y)}{y_{\mathrm{m}}^2} R\left(\frac{y}{y_{\mathrm{m}}}; b, g\right), \tag{18}$$

where R is a 10th-order even polynomial,

$$R(x; b, g) = \sum_{k=0}^{5} B_k(b, g) x^{2k}, \tag{19}$$

whose coefficients are given by Horner's scheme as

$$B_5 = B_4 = B_3 = 4y_{\mathrm{m}}^{12}; \qquad B_2 = B_1 = B_3 - 4y_{\mathrm{m}}^6; \qquad B_0 = g^2. \tag{20}$$

Inserting $u = 2\sin^{-1}(y/y_{\mathrm{m}})/\pi$ transforms Eq. (9) to

$$\frac{\chi(b, g)}{\pi} = 1 - bgy_{\mathrm{m}} \int_0^1 \frac{du}{\sqrt{R(\sin\frac{1}{2}\pi u; b, g)}}. \tag{21}$$

This integrand is finite across its domain when P has just one root. When b and g are on the orbit line, however, poles of order 1 or 2 occur at $u = 1$; then $\chi \to -\infty$.

Hirschfelder et al. [9,25–27] replaced the integrand in their equivalent of Eq. (21) with a best-fit polynomial. This injected numerical error without specific bounds. Akhmatskaya and Pozhar [15] brought more rigor to the analysis, using Gauss–Chebyshev quadrature to approximate the integral with bounded error [41].

For the present work a 4th-order Runge–Kutta method (RK4) [39] was adapted to perform the integration in Eq. (21). Grid-independent values valid to machine precision were extrapolated by using the known dependence of error on mesh spacing in the RK4 scheme. Results matched those of Colonna and Laricchiuta's fractal integration algorithm [1], which yields results of similar accuracy at considerably greater computational expense.

Fig. 4 maps out the characteristic shapes of trajectories with respect to the impact parameter b and relative speed g. Although this sort of map can greatly aid the physical understanding of pair potentials, to the best of our knowledge, Fig. 4 is

Table 3
Comparison of calculated deflection angles to literature data.

$g^2 = 0.1$	Deflection angle χ (radian)			Region in Fig. 4
b	Hirschfelder et al. [9]	Sharipov and Bertoldo[a] [42]	This work	
2.838	−0.323	−0.3230	−0.3230	III
2.696	−0.543	−0.5435	−0.5435	III
2.643	−0.706	−0.7049	−0.7049	III
2.598	−0.945	−0.9437	−0.9437	III
2.572	−1.205	−1.199	−1.199	III
2.544	−1.998	−1.977	−1.977	III
2.539	−2.576	−2.584	−2.584	III
2.538	−2.346	−2.903	−2.903	III
2.516	−1.166	−4.481	−4.481	V
2.503	−1.944	−3.959	−3.959	V
2.470	−2.867	−3.202	−3.203	V
2.456	−3.106	−2.984	−2.984	IV
2.400	−2.509	−2.356	−2.356	IV
2.328	−1.943	−1.819	−1.819	IV
2.171	−1.124	−1.041	−1.041	IV
1.996	−0.491	−0.4360	−0.4360	IV
1.881	−0.150	−0.1119	−0.1119	IV

[a] Definition of χ adjusted to match Hirschfelder et al.'s convention [9].

the first topological diagram of its kind. Four lines demarcate regions where 'collisions' ($0 \leq \chi$), 'deflections' ($-\pi \leq \chi < 0$), 'loops' ($\chi < -\pi$) and orbits ($\chi \to -\infty$) occur. Trajectories can also have inflection points, introducing another line that ultimately partitions the map into six domains.

Representative trajectories obtained by solving Eq. (5) are included in each region that occupies finite area on the map. In regions I and II of Fig. 4, the impact parameter is relatively small; particles therefore collide with a trajectory dominated by short-range repulsion. Some effect of attraction is seen for trajectories in region I, where kinetic energy (which scales as g^2) is lower. In regions III and IV, the impact parameter is relatively large, so interactions are dominated by long-range attraction, which ultimately causes the incoming particle to be deflected toward the incident particle from its original path. In region III, the kinetic energy is large enough that repulsion does not have a significant effect; incoming gas particles primarily experience long-range attraction. When kinetic energy is smaller, in region IV, the particles are drawn sufficiently close together by the attractive force that repulsion comes into effect. In regions V and VI, kinetic energy is low enough that particles spiral around each other one or more times before the attractive force can be overcome. Qualitatively dissimilar loops appear above and below the orbit line, in regions V and VI, respectively.

Table 3 compares numerical computations reported by Hirschfelder et al. [9] and Sharipov and Bertoldo [42] to the first four significant digits (the highest precision reported in previous work) of the grid-independent deflection angles computed using the extrapolative RK4 algorithm described above. The squared relative speed g^2 is fixed to 0.1, and the impact parameter b is varied to pass through regions III, IV, and V. Note that deflection angles reported in Ref. [42] were adjusted to match Hirschfelder et al.'s convention for expressing χ.

Results from extrapolative RK4 differ significantly from those of Hirschfelder et al. But they are almost identical to Sharipov and Bertoldo's, excepting one value at $b = 2.470$, which disagrees in the third digit past the decimal. It is worth noting that this point is the closest to the orbit line in the table. This minute difference may owe to the method by which Sharipov and Bertoldo evaluated deflection angles, which involved splitting Eq. (9) into two integrations; in one integration domain P was linearized around its roots. In regions V and VI of the trajectory map the second derivative of P can be larger than its first, and quadratic behavior of P dominates. Thus one should be careful when applying Sharipov and Bertoldo's method of linearization near singularities, which may be subject to small errors when trajectories exhibit loops.

Inflections occur when $d^2\theta/dy^2$ changes sign during an encounter, which happens only if dP/dy changes sign. Either dP/dy has two real positive roots or it has none [37,38]. These domains of b and g are separated by a line where the root repeats, which can be found by Akhmatskaya and Pozhar's method [15] to be $bg = 6/\sqrt[6]{3125}$ (the 'inflection line' in Fig. 4). Roots of dP/dy must also be less than y_m to yield inflected trajectories, so the orbit line also bounds regions I, IV, and V in Fig. 4.

Orbiting trajectories and those in regions I, III, IV and VI are well documented [1,9,15,25,27,29,42–44], but to the best of our knowledge regions II and V have not been discussed. Region V is most important because looping trajectories dramatically affect collision cross-sections.

3.4. Collision cross section

Divergent deflection angles make the integrand of the reduced cross section $Q^{(l)\star}$ take on fractal character, oscillating with unboundedly increasing frequency as the orbit line is approached. The integrand in Eq. (10) is not Riemann integrable in the neighborhood of b_o (cf. Eq. (15)); at b_o, it is undefined. Earlier analyses approximate χ near the orbit line, taking $\chi \propto 1/\sqrt{b^2 - b_o^2(g)}$, and using the proportionality constant as a fitting parameter. This accounts neither for the discontinuity
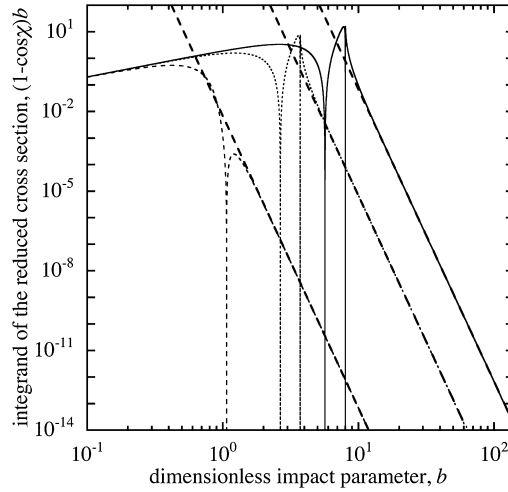
Fig. 5. Integrands of the reduced cross sections, $Q^{(l)\star}$, and the asymptotic behavior for $b \gg 1$, with $l = 1$. Solid line, $g = 0.001$; dotted line, $g = 0.1$; short dashed line, $g = 10$; long-dashed lines show the asymptotic behavior from Eq. (23).

in nor the non-analyticity of $\cos \chi$ near b_o. Even the most authoritative earlier sources [15,25] do not address the error this approximation incurs.

An *ad hoc* Lebesgue integration can be used to circumvent problems associated with non-analyticity of the integrand in Eq. (10) at the orbit line. A measure of the error in the integral's value as it crosses b_o is provided by cutting out a small area of the integration domain around b_o, $b \in [b_o - \delta, b_o + \delta]$. In any region of the trajectory map, the upper bound of the integrand in Eq. (10) is b for even l and $2b$ for odd l; its lower bound is always zero. Thus the exclusion of a neighborhood of size 2δ around b_o induces an error in resulting $Q^{(l)\star}$ values of at most $2\delta b_o$ for even l and $4\delta b_o$ for odd l. It follows that numerical error in the integral as a whole can be controlled by the choice of δ; an exact integral can be calculated in principle by taking a limit as the measure δ goes to zero.

To resolve difficulties with the semi-infinite integration domain in Eq. (10), observe that integrands in $Q^{(l)\star}$ always behave similarly when impact parameters are large. Asymptotic behavior was analyzed to inform a decision procedure for terminating the upper bound of the integration domain at a predefined level of accuracy. The asymptotic analysis begins with Eqs. (6) and (16). When b is much greater than 1, P asymptotically satisfies

$$\lim_{b \gg 1} P(y_m) = g^2 \left(1 - b^2 y_m^2\right) + 4 y_m^6 + O\left(\frac{1}{b^{12}}\right). \tag{22}$$

An asymptotic formula for y_m follows from Eq. (8). Insertion into Eqs. (18), (20), and (21) yields the asymptotic behavior of the deflection angle. Maclaurin expansion of the cosine ultimately provides the formula

$$\lim_{b \gg 1} \left(1 - \cos^l \chi\right) b = \frac{225 \pi^2 l}{32 g^4 b^{11}} + O\left(\frac{1}{b^{17}}\right). \tag{23}$$

The collision-cross-section integrand and Eq. (23) are depicted in Fig. 5; they match if b is sufficiently large.

Eq. (23) allows estimation of the error induced by truncating the integration domain in Eq. (10) at finite upper bound b_{stop}. Presuming that $b_{stop} \gg 1$, the portion of the semi-infinite integral lost is

$$\int_{b_{stop}}^{\infty} \left[\lim_{b \gg 1} \left(1 - \cos^l \chi\right) b\right] db = \frac{45 \pi^2 l}{64 g^4 b_{stop}^{10}} + O\left(\frac{1}{b_{stop}^{16}}\right). \tag{24}$$

Marching forward from $b = 0$ with RK4, the ratio of the area lost by truncation of the domain to the area already integrated can be monitored to decide when to halt the numerical procedure.

Fig. 6 compares collision cross sections previously reported by Hirschfelder et al. [25] and Storck [43] to those developed here, as functions of the dimensionless kinetic energy g^2. For the present calculations an error tolerance of 1×10^{-8} (yielding computed results accurate to seven digits past the decimal) was deemed sufficient. The inset in Fig. 6 shows significant differences between the present results and Storck's for a range of g^2 values between 0.5 and 2.0. These differences owe to Storck's neglect of the consequences of looping trajectories (in regions V and VI of Fig. 4).

3.5. Collision integrals

The reduced collision integrals $\Omega^{(l,s)\star}$ defined in Eq. (11) are more readily computed than other preliminary quantities. Although the integration domain is also semi-infinite, the integrand decreases rapidly with g^2, making it easier to create
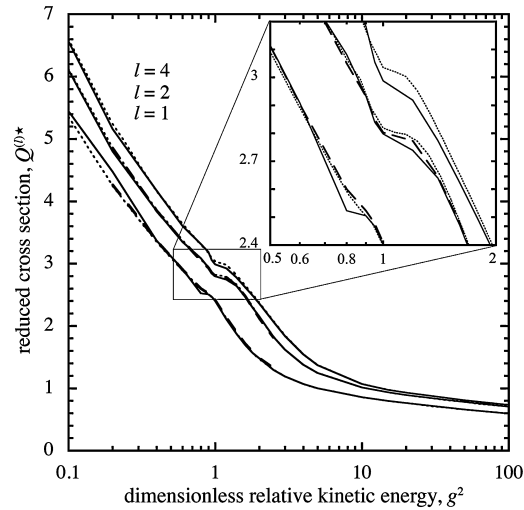
Fig. 6. Collision cross section $Q^{(l)\star}$ as a function of relative kinetic energy g^2. The solid lines are reprinted from Hirschfelder et al. [25]; the dashed lines are from Storck [43]; the dotted lines represent calculations accurate to 6 digits based on the methods discussed here. The inset shows significant differences when g^2 is near unity.

Table 4
Comparison of LJ (12–6) collision integrals from literature and this work.

T^*	$\Omega^{(l,s)\star}$	Hirschfelder et al. [9]	Sharipov and Bertoldo [42]	Empirical interpolation Eq. (1)	High-precision algorithm, error $O(10^{-8})$
0.3	(1, 1)	2.662	2.650	2.6500	2.6500024
	(1, 2)	2.256	2.257	2.2568	2.2568342
	(1, 3)	1.962	1.966	1.9665	1.9665277
	(2, 2)	2.785	2.844	2.8436	2.8436719
	(2, 3)	2.535	2.581	2.5806	2.5806610
	(2, 4)	2.333	2.362	2.3623	2.3622719
	(2, 5)	2.152	2.170	2.1704	2.1704207
	(2, 6)	1.990	2.001	2.0011	2.0010465
	(4, 4)	2.557	2.571	2.5710	2.5710549
400	(1, 1)	0.4170		0.41418	0.41418524
	(1, 2)	0.3955		0.39190	0.39188997
	(1, 3)	0.3802		0.37599	0.37598843
	(2, 2)	0.4811		0.47103	0.47103246
	(2, 3)	0.4638		0.45228	0.45226789
	(2, 4)	0.4502		0.43778	0.43777361
	(2, 5)	0.4393		0.42604	0.42603617
	(2, 6)	0.4302		0.41622	0.41621633
	(4, 4)	0.4758		0.45890	0.45888704

procedures to terminate the integration with bounded error. The super-exponentially decreasing character of the integrand allows precision to be insured by a procedure where the forward-marching RK4 integration is halted when the integrand becomes smaller than a target value.

Collision integrals accurate to seven digits past the decimal are compared to previously reported values at two reduced temperatures, $T^* = 0.3$ and 400, in Table 4. The results of empirical interpolation formulas from Eq. (1) with parameters from Table 1 are also shown for comparison. Both the high-precision and interpolated collision integrals agree with Sharipov and Bertoldo's up to the precision they reported [42].

More collision integrals at different dimensionless temperature are tabulated in the supplementary material. Eq. (1) was obtained by fitting the entries of that table using the method of least squares, as discussed in Section 2. As a result, Eq. (1) generates collision integrals accurate to at least four significant digits when $0.3 \leq T^* \leq 400$. Collision integral values generated using Eq. (1) should suffice for most continuum heat, mass, and momentum transport analyses.

The present computations in the last column deviate up to 2% from those of Hirschfelder et al., consistent with the observation of Akhmatskaya and Pozhar [15]. In addition, there is a larger difference, up to 3.5%, at $T^* = 400$. This is consistent with NJA's observation that previous computations were in error at large T^* [17]. There is general agreement with the collision integrals provided by Sharipov and Bertoldo [42]. Note that in addition to having dramatically reduced computation times, the interpolation formulas provide accuracy that is well within the bounds of intrinsic experimental error associated with most laboratory transport-property measurement techniques.

4. Lennard-Jones parameters for neon, argon, and krypton

Finding the pair potential that best describes a particular type of particle is a challenging inverse problem. The temperature dependences of various properties are in principle known from experiments, with various degrees of measurement error. Parameterization of a potential requires that all of these observed dependences be simultaneously matched using calculations from kinetic theory—or at least, it should. A true optimization of LJ parameters using transport and thermodynamic properties together has not yet been performed, because iterative procedures involving transport properties require prohibitively time-intensive collision-integral calculations.

Previous efforts to establish LJ pair potentials in gases have also tended to use one set of property data, such as the second virial coefficient [45] or viscosity [25], and varied both LJ parameters in an *ad hoc* fashion to obtain a best fit. Recently, similar attention has been given to the matching of spectroscopic data [12]. Such procedures do not guarantee a choice of potential parameters that minimizes the error across multiple properties.

It is worth mentioning that many papers—both classical and modern—call into question whether the LJ potential accurately models gas–particle interactions at all [13,14,18,46–48]. When considering such criticisms, it should be borne in mind that the true test of a potential model is whether it accurately predicts how macroscopic thermodynamic and transport properties depend on temperature—with 'accurately' taken to mean 'within the bounds of intrinsic experimental error for all known data at all accessible temperatures.' Since accurate collision-integral tables have never been used for this sort of multi-objective optimization of the LJ potential, it is impossible to judge whether or not the potential models any actual gas well. To address this concern, simultaneous best fits of the two most accurately known properties (second virial coefficient and viscosity) of gases were used to parameterize the LJ potential; the predictive capability of the potential was then tested by comparison to less accurately known properties (thermal conductivity and self-diffusion coefficient). All four properties for Ne, Ar, and Kr were matched by a LJ potential within experimental error. Properties could not be simultaneously matched for He and Xe, as further discussed below.

Virial coefficients are thermodynamic properties. By definition, they correct the pressure-explicit equation of state for an ideal gas according to

$$\frac{p\overline{V}}{N_A k_B T} = 1 + \frac{B_{2V}(T)}{\overline{V}} + \frac{B_{3V}(T)}{\overline{V}^2} + \dots, \tag{25}$$

in which the second coefficient B_{2V} reflects pairwise interactions, the third virial coefficient B_{3V} quantifies pairwise and three-body interactions, *etc.* [49]. Here p is pressure, $\overline{V}$ is the molar volume, and N_A is Avogadro's number. In a pure gas B_{2V} varies with temperature as [50]

$$B_{2V}(T^*) = 2\pi\sigma^3 N_A \int_0^\infty \frac{1}{y^4}\big[e^{-\frac{\phi'(\sigma/y)}{\epsilon T^*}} - 1\big]dy. \tag{26}$$

Lennard-Jones considered a number of pair potentials, ultimately settling on the form in Eq. (4) [51,52].

Transport coefficients depend on collision integrals of various orders, which in turn depend on the pair potential. Hirschfelder et al. implemented one of the first attempts to determine LJ parameters from a transport property—viscosity. The viscosity η is given terms of collision integrals for an LJ gas as [9]

$$\eta(T^*) = \frac{5\sqrt{\pi\epsilon m T^*}}{16\pi\sigma^2\Omega^{(2,2)\star}(T^*)} f_\eta^{(n)}. \tag{27}$$

Here $f_\eta^{(n)}$ denotes a function that brings η up to the nth order in the Sonine expansion. The thermal conductivity k and self-diffusion coefficient $\mathscr{D}$ are

$$k(T^*) = \frac{75 k_B}{64\sigma^2\Omega^{(2,2)\star}(T^*)}\sqrt{\frac{\epsilon T^*}{\pi m}} f_k^{(n)} \quad \text{and} \tag{28}$$

$$\mathscr{D}(T^*) = \frac{3\sqrt{\pi\epsilon m T^*}}{8\pi\sigma^2\rho(T^*, p)\Omega^{(1,1)\star}(T^*)} f_{\mathscr{D}}^{(n)}, \tag{29}$$

where $f_k^{(n)}$ and $f_{\mathscr{D}}^{(n)}$ represent corrections of nth order. Since it involves the density ρ, given up to second order in the virial expansion by

$$\rho(T^*, p) = \frac{m N_A}{2 B_{2V}(T^*)}\left[-1 + \sqrt{1 + \frac{4 p B_{2V}(T^*)}{\epsilon N_A T^*}}\right], \tag{30}$$

computation of the self-diffusion coefficient $\mathscr{D}$ involves calculating B_{2V} as well as collision integrals.

Use of higher-order corrections improves accuracy of the property in question, but only up to a point—Viehland et al. [53] demonstrated that convergence of the approximation is ordinarily very rapid, and that third- and fourth-order calculations of the viscosity in the dimensionless temperature range $0.3 \leq T^* \leq 400$ differ by less than 0.004%, far less than the 2.5%
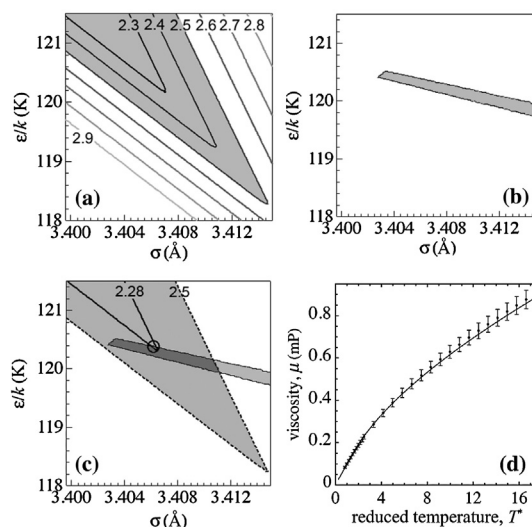
Fig. 7. Procedure for LJ parameterization of argon: (a) contours of the maximum percentage deviation between theoretical and calculated viscosity values (the viscosity-correct region where calculations match experiments is shaded); (b) virial-correct region; (c) contraction of the viscosity-correct region to minimize error in viscosity within dual-correct region; (d) comparison of results to experiments.

experimental error in typical viscosity measurement. Hurly and Moldover showed that third- and fourth-order calculations of thermal conductivity differ by less than 0.01% over a wide temperature range [54]. For this work, $f_\eta^{(3)}$, $f_k^{(3)}$, and $f_\mathscr{D}^{(2)}$ were deemed sufficiently accurate to facilitate Lennard-Jones parameterization. These functions are written in terms of collision integrals in Appendix A.

An LJ parameterization effort requires reliable experimental data that quantify the temperature dependences of B_{2V}, η, k, and $\mathscr{D}$. Here 'reliable' is interpreted to mean that the experiments were replicated and reported with quantitative estimates of experimental error. Maitland and Smith [55] performed an extensive data search for gas viscosities, and aggregated literature data to generate tables with reported accuracy of 2.5% for the viscosities of Ne, Ar, and Kr between their boiling points and 2000 K. Saxena et al.'s data were used for thermal conductivities between 350 K and 1500 K, which have 4.0% maximum error [56–59].

Measurements of both self-diffusion coefficients [60–64] and mutual-diffusion coefficients [65,66] at atmospheric pressure were collected. Mutual diffusion coefficients were converted to self-diffusion coefficients by correcting m for the composition differences between equilibrated isotopic-mixture compositions and naturally occurring isotope ratios. Some reports do not provide error estimates [63–65]; most report error of a few percent.

The extensive tables produced by Dymond and Smith [67], which compile measurements by numerous groups over several decades, were used as the source of B_{2V} data. Error ranges for second virial coefficients are typically provided as absolute values, rather than percentages, on the basis that B_{2V} is very close to zero when gases behave near ideally. Error in B_{2V} ranges from 0.5–1 cm^3/mol.

Experimental data quantifying the temperature dependences of viscosity η and second virial coefficient B_{2V} were fit with Eqs. (26) and (27), using Eqs. (31) and (32) to get $f_\eta^{(3)}$ in terms of collision integrals, and Eq. (1) for collision-integral computation. This approach uses both a thermodynamic property and a transport property—parameters computed by two disparate theories. Among transport coefficients, viscosity was chosen as the objective for LJ parameterization because it has the least error and is known over the widest temperature range.

LJ parameter optimization was facilitated by a graphical method, illustrated in Fig. 7 for Ar. A contour plot of the maximum percentage deviation from experimental η values was created vs. σ and ϵ/k_B. The experimental error of 2.5% corresponds to one of these contours, delineating a 'viscosity-correct' region in which all combinations of σ and ϵ/k_B correctly predict the temperature dependence of viscosity. In a similar plot for B_{2V}, a 'virial-correct' region was identified by creating a Boolean function that took value 1 if all predicted B_{2V} values for a given σ and ϵ/k_B were within experimental error, and 0 otherwise, and coloring the two values differently. Any σ and ϵ/k_B values within the intersection of the 'viscosity-correct' and 'virial-correct' regions match both properties within error. Since this overlap is finite, a constraint is needed to determine 'exact' parameter values. Viscosities are more precisely measured, so the deviation from viscosity data within this 'dual-correct' domain was minimized: the error tolerance on the 'viscosity-correct' domain was reduced until it met the 'virial-correct' domain within the precision of Eq. (1).

Property data for helium and xenon were also tested, but for these gases, the 'virial-correct' and 'viscosity-correct' domains were found not to overlap. It was concluded that the LJ potential does not suffice to implement property correlation for these gases, and they were consequently excluded from the study. (It is well known that quantum effects are significant in He at low temperature, and that multi-atom clusters commonly arise in Xe.) Ab initio potentials would be expected to provide better matches for temperature-dependent properties of He and Xe [13,14].
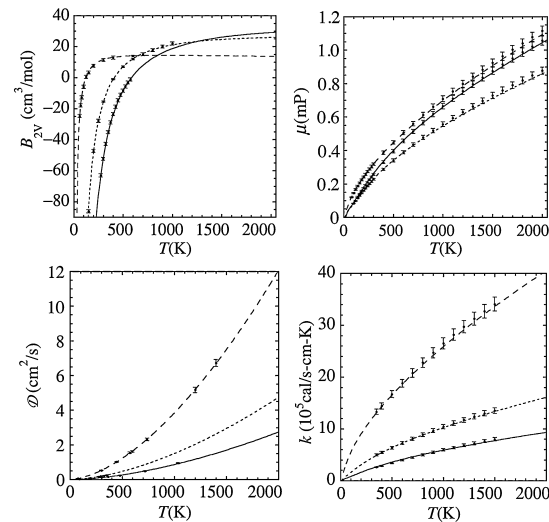
Fig. 8. Optimal LJ parameters generate four different gas properties accurately within experimental error. Each graph includes three gases: neon (dashed), argon (dotted), and krypton (solid). Data for $\mathscr{D}$ are at 101 325 Pa.

Table 5
Comparison of LJ parameters from this work to literature values for Ne, Ar, and Kr, showing average and maximum deviation from measured transport properties, as well as the number of points located inside the virial-correct region in Fig. 7. Intrinsic experimental errors are written parenthetically next to η, k, and $\mathscr{D}$.

Gas	Group	Properties used for parameterization	ϵ/k_B (K)	σ (Å)	η (2.5%)		k (4%)		$\mathscr{D}$ ($\geq$3%)		B_{2V}
					avg	max	avg	max	avg	max	
Ne	Lennard-Jones	B_{2V}	35.35	2.743	2.6	5.3	1.3	2.2	2.8	4.3	6/10
	Hirschfelder	η	35.7	2.80	1.3	2.2	3.0	3.7	0.7	1.4	8/10
	Kestin	η	60.89	2.6481	1.3	8.8	0.4	0.7	2.4	12.	0/10
	This work	η, B_{2V}	35.750	2.7820	1.3	2.0	1.7	2.5	0.7	1.5	10/10
Ar	Lennard-Jones	B_{2V}	119.5	3.408	1.8	2.5	1.2	2.1	1.1	2.6	10/11
	Hirschfelder	η	124.0	3.418	2.0	3.4	2.4	3.2	1.3	3.2	3/11
	Kestin	η	152.75	3.2923	1.4	6.4	1.3	2.1	2.2	7.5	0/11
	This work	η, B_{2V}	120.38	3.4062	1.8	2.3	1.2	2.1	1.1	2.4	11/11
Kr	Hirschfelder	η	190.0	3.61	2.1	3.3	2.1	4.5	2.2	4.4	0/13
	Kestin	η	206.42	3.5222	1.1	2.8	1.8	3.9	1.3	2.2	0/13
	This work	η, B_{2V}	171.64	3.6202	1.5	2.5	2.4	3.9	1.4	3.0	13/13

For Ne, Ar, and Kr, validity of the optimized LJ parameters was tested by using parameters fit to η and B_{2V} to predict k and $\mathscr{D}$; the predictions were subsequently compared to experimental data. Thermal conductivity correlates strongly to viscosity. The self-diffusion coefficient more stringently tests a potential model, because in addition to depending on a different order of collision integral than viscosity, its raw experimental value also depends on the second virial coefficient.

Fig. 8 compares theory and experiments. LJ parameters determined by the procedure above match all available reliable η and B_{2V} data within experimental error by design; the parameters so found also match all reliable k and $\mathscr{D}$ data.

LJ (12–6) parameters for Ne, Ar, and Kr are presented in Table 5. The table also provides data from canonical sources who used transport and/or thermodynamic property data to parameterize the potential [9,45,68]. Ironically, Lennard-Jones' parameters (the oldest) are closer to the ones obtained here than any others, because Lennard-Jones based his parameter optimization on the second virial coefficient alone, avoiding a reliance on error-prone collision-integral computation. Hirschfelder et al. suggested that their LJ parameters would describe pair potentials better because of the lower intrinsic error of viscosity measurements. Table 5, however, shows that Hirschfelder et al. found inaccurate LJ parameters due to faulty collision-integral calculations. DiPippo and Kestin's more recent LJ parameterization [68] was based on the collision-integral tables of Hirschfelder et al., and is therefore similarly suspect.

5. Conclusion

An arbitrary-precision algorithm was developed to calculate collision integrals for the LJ (12–6) potential. To speed computation and solve inverse problems with variable LJ parameters, interpolation formulas accurate to at least four digits of precision were developed (Eq. (1)). LJ parameters were computed for three gases by simultaneously fitting experimental data for the temperature dependence of viscosity and second virial coefficient. Collision integrals were involved in viscosity

calculation, and the second virial coefficient came from a separate equilibrium theory. The LJ parameters that matched these properties were verified using the self-diffusion coefficient and thermal conductivity of the gases in question. LJ potentials were found that predict the temperature dependences of viscosities, thermal conductivities, self-diffusion coefficients, and second virial coefficients of dilute neon, argon, and krypton, from their boiling points up to 2000 K.

Acknowledgements

Appendix A

The third-order viscosity correction includes a factor

$$f_\eta^{(3)} = 1 + \frac{b_{12}^2}{b_{11}b_{22} - b_{12}^2} + \frac{b_{11}(b_{12}b_{23} - b_{22}b_{13})^2}{(b_{11}b_{22} - b_{12}^2)\det(\mathbf{b})}, \tag{31}$$

where the independent entries in the 3×3, symmetric matrix $\mathbf{b}$ are

$$b_{11} = 4\Omega^{(2,2)\star}$$
$$b_{12} = 7\Omega^{(2,2)\star} - 8\Omega^{(2,3)\star}$$
$$b_{22} = \frac{301}{12}\Omega^{(2,2)\star} - 28\Omega^{(2,3)\star} + 20\Omega^{(2,4)\star}$$
$$b_{13} = \frac{63}{8}\Omega^{(2,2)\star} - 18\Omega^{(2,3)\star} + 10\Omega^{(2,4)\star}$$
$$b_{23} = \frac{1365}{32}\Omega^{(2,2)\star} - \frac{321}{4}\Omega^{(2,3)\star} + \frac{125}{2}\Omega^{(2,4)\star} - 30\Omega^{(2,5)\star}$$
$$b_{33} = \frac{25\,137}{256}\Omega^{(2,2)\star} - \frac{1755}{8}\Omega^{(2,3)\star} + \frac{1905}{8}\Omega^{(2,4)\star} - 135\Omega^{(2,5)\star} + \frac{105}{2}\Omega^{(2,6)\star} + 12\Omega^{(4,4)\star}. \tag{32}$$

The same order of thermal conductivity involves

$$f_k^{(3)} = 1 + \frac{a_{12}^2}{a_{11}a_{22} - a_{12}^2} + \frac{a_{11}(a_{12}a_{23} - a_{22}a_{13})^2}{(a_{11}a_{22} - a_{12}^2)\det(\mathbf{a})}, \tag{33}$$

where entries in the symmetric 3×3 matrix $\mathbf{a}$ are

$$a_{11} = b_{11}; \qquad a_{12} = b_{12}; \qquad a_{13} = b_{13};$$
$$a_{22} = \frac{77}{4}\Omega^{(2,2)\star} - 28\Omega^{(2,3)\star} + 20\Omega^{(2,4)\star}$$
$$a_{23} = \frac{945}{32}\Omega^{(2,2)\star} - \frac{261}{4}\Omega^{(2,3)\star} + \frac{125}{2}\Omega^{(2,4)\star} - 30\Omega^{(2,5)\star}$$
$$a_{33} = \frac{14\,553}{256}\Omega^{(2,2)\star} - \frac{1215}{8}\Omega^{(2,3)\star} + \frac{1565}{8}\Omega^{(2,4)\star} - 135\Omega^{(2,5)\star} + \frac{105}{2}\Omega^{(2,6)\star} + 4\Omega^{(4,4)\star}. \tag{34}$$

Second-order self-diffusion coefficients include

$$\frac{1}{f_{\mathscr{D}}^{(2)}} = 1 - \frac{(6C^\star - 5)^2}{55 - 12B^\star + 16A^\star}, \tag{35}$$

where

$$A^\star = \Omega^{(2,2)\star} / \Omega^{(1,1)\star}$$
$$B^\star = \left[5\Omega^{(1,2)\star} - 4\Omega^{(1,3)\star}\right] / \Omega^{(1,1)\star}$$
$$C^\star = \Omega^{(1,2)\star} / \Omega^{(1,1)\star}. \tag{36}$$

These orders of η, k, and $\mathscr{D}$ suffice to fit all the available data for the gases discussed in this article.

Appendix B. Supplementary material

Supplementary material related to this article can be found online at http://dx.doi.org/10.1016/j.jcp.2014.05.018.

References

[1] G. Colonna, A. Laricchiuta, General numerical algorithm for classical collision integral calculation, Comput. Phys. Commun. 178 (2008) 809–816.
[2] R. Eslamloueyan, M. Khademi, A neural network-based method for estimation of binary gas diffusivity, Chemom. Intell. Lab. Syst. 104 (2010) 195–204.
[3] L. Boltzmann, Lectures on Gas Theory (trans. S.G. Brush), University of California Press, 1964.
[4] R.B. Bird, W.E. Stewart, E.N. Lightfoot, Transport Phenomena, 2nd ed., Wiley, 2001.
[5] P.T. Gressman, R.M. Strain, Global classical solutions of the Boltzmann equation with long-range interactions, Proc. Natl. Acad. Sci. USA 107 (2010) 5744–5749.
[6] D. Enskog, Kinetische Theorie der Vorgänge in mässig verdünnten Gasen, Ph.D. thesis, Uppsala, Sweden, 1917.
[7] S. Chapman, On the kinetic theory of a gas. Part II: a composite monatomic gas: diffusion, viscosity, and thermal conduction, Philos. Trans. R. Soc. Lond. A 217 (1918) 115–197.
[8] S. Chapman, T.G. Cowling, The Mathematical Theory of Non-uniform Gases, Cambridge University Press, 1939.
[9] J. Hirschfelder, C. Curtiss, R.B. Bird, Molecular Theory of Gases and Liquids, J. Wiley & Sons, New York, 1963. *inaccurate integrals*
[10] S. Harris, An Introduction to the Theory of the Boltzmann Equation, Holt, Rinehart, and Winston, 1971.
[11] G.C. Maitland, M. Rigby, E.B. Smith, W.A. Wakeham, Intermolecular Forces: Their Origin and Determination, Clarendon Press, 1981.
[12] R.A. Aziz, R. Janzen, R.O. Simmons, Rare gases, in: G.L. Trigg (Ed.), Encyclopedia of Applied Physics, Wiley, 2004.
[13] B. Jaeger, R. Hellmann, E. Bich, E. Vogel, Ab initio pair potential energy curve for the argon atom pair and thermophysical properties for the dilute argon gas. I. Argon–argon interatomic potential and rovibrational spectra, Mol. Phys. 107 (2009) 2181–2188.
[14] F. Sharipov, J.L. Strapasson, *Ab initio* simulation of transport phenomena in rarefied gases, Phys. Rev. E 86 (2012) 031130.
[15] E.V. Akhmatskaya, L.A. Pozhar, Calculation of transport collision integrals for a Lennard-Jones gas, USSR Comput. Math. Math. Phys. 26 (1986) 185–190.
[16] U.R. Hattikudur, G. Thodos, Equations for the collision integrals $\Omega^{(1,1)*}$ and $\Omega^{(2,2)*}$, J. Chem. Phys. 52 (1970) 4313. *inaccurate integrals*
[17] P.D. Neufeld, A.R. Janzen, R.A. Aziz, Empirical equations to calculate 16 of the transport collision integrals $\Omega^{(l,s)*}$ for the Lennard-Jones (12–6) potential, J. Chem. Phys. 57 (1972) 1100–1102. *inaccurate integrals*
[18] E.A. Mason, Higher approximations for the transport properties of binary gas mixtures. II. Applications, J. Chem. Phys. 27 (1957) 782–790.
[19] H. O'Hara, F.J. Smith, Transport collision integrals for a dilute gas, Comput. Phys. Commun. 2 (1971) 47–54.
[20] S.J. Leon, Linear Algebra with Applications, 4th ed., Macmillan Coll. Div., 1994.
[21] K.W. Ford, J.A. Wheeler, Semiclassical description of scattering, Ann. Phys. 7 (1959) 259–286.
[22] F.J. Smith, R.J. Munn, Automatic calculation of the transport collision integrals with tables for the Morse potential, J. Chem. Phys. 41 (1964) 3560–3568.
[23] S. Imam-Rahajoe, C.F. Curtiss, R.B. Bernstein, Numerical evaluation of quantum effects on transport cross sections, J. Chem. Phys. 42 (1965) 530–536.
[24] H. Grad, On the kinetic theory of rarefied gases, Commun. Pure Appl. Math. 2 (1949) 331–407.
[25] J.O. Hirschfelder, R.B. Bird, E.L. Spotz, The transport properties for non-polar gases, J. Chem. Phys. 16 (1948) 968–981.
[26] J.O. Hirschfelder, R.B. Bird, E.L. Spotz, The transport properties for non-polar gases, J. Chem. Phys. 17 (1949) 1343–1344.
[27] J.O. Hirschfelder, R.B. Bird, E.L. Spotz, The transport properties of gases and gaseous mixtures. II, Chem. Rev. 44 (1949) 205–231.
[28] V.J. Berry Jr., R.C. Koeller, Diffusion in compressed binary gaseous systems, AIChE J. 6 (1960) 274–280.
[29] M. Kotani, Determination of intermolecular forces from transport phenomena in gases, Proc. Phys. Math. Soc. Jpn. 3rd Ser. 24 (1942) 76–95.
[30] T. Kihara, M. Kotani, Determination of intermolecular forces from transport phenomena in gases. II, Proc. Phys. Math. Soc. Jpn. 3rd Ser. 25 (1943) 602–614.
[31] J.S. Rowlinson, The transport properties of non-polar gases, J. Chem. Phys. 17 (1949) 101.
[32] J.E. Lennard-Jones, On the forces between atoms and ions, Proc. R. Soc. Lond. A 109 (1925) 584–597.
[33] J.E. Lennard-Jones, B.M. Dent, The forces between atoms and ions. II, Proc. R. Soc. Lond. Ser. A 112 (1926) 230–234.
[34] F. London, Zur Theorie und Systematik der Molekularkräfte, Z. Phys. A 63 (1930) 245–279.
[35] R. Eisenschitz, F. London, Über das Verhältnis der van der Waalsschen Kräfte zu den homöopolaren Bindungskräften, Z. Phys. A, Hadrons Nucl. 60 (1930) 491–527.
[36] H. Hettema, Quantum Chemistry: Classic Scientific Papers, World Scientific, Singapore, 2000.
[37] G. Hostetter, Using the Routh–Hurwitz test to determine numbers and multiplicities of real roots of polynomial, IEEE Trans. Circuits Syst. 22 (1975) 697–698.
[38] G. Hostetter, Additional comments on "On the Routh–Hurwitz criterion", IEEE Trans. Autom. Control 20 (1975) 296–297.
[39] W.H. Press, Numerical Recipes in FORTRAN, Cambridge University Press, 1992.
[40] W.G. Horner, A new method of solving numerical equations of all orders, by continuous approximation, Philos. Trans. R. Soc. Lond. 109 (1819) 308–335.
[41] V.I. Krylov, Approximate Calculation of Integrals, Macmillan, 1962.
[42] F. Sharipov, G. Bertoldo, Numerical solution of the linearized Boltzmann equation for an arbitrary intermolecular potential, J. Comput. Phys. 228 (2009) 3345–3357.
[43] U. Storck, Computation of the transport coefficients of polar gases using verified numerical integration, Z. Angew. Math. Mech. 78 (1998) 555–563.
[44] G.A.L. Delvigne, J. Los, Numerical calculation of the classical deflection function, Physica 63 (1973) 339–350.
[45] J. Lennard-Jones, The equation of state of gases and critical phenomena, Physica 4 (1937) 941–956.
[46] J. Kestin, K. Knierim, E.A. Mason, B. Najafi, S.T. Ro, M. Waldman, Equilibrium and transport properties of the noble gases and their mixtures at low density, J. Phys. Chem. Ref. Data 13 (1984) 229–303.
[47] E.A. Mason, W.E. Rice, The intermolecular potentials of helium and hydrogen, J. Chem. Phys. 22 (1954) 522–535.
[48] E.A. Mason, Transport properties of gases obeying a modified Buckingham (exp, 6) potential, J. Chem. Phys. 22 (1954) 169–186.
[49] J. McCabe, S. Ouvry, Perturbative three-body spectrum and the third virial coefficient in the anyon model, Phys. Lett. B 260 (1991) 113–119.
[50] H.L. Frisch, E. Helfand, Conditions imposed by gross properties on the intermolecular potential, J. Chem. Phys. 32 (1960) 269–270.
[51] J.E. Jones, On the determination of molecular fields. I. From the variation of the viscosity of a gas with temperature, Proc. R. Soc. Lond. A 106 (1924) 441–462.
[52] J.E. Jones, On the determination of molecular fields. II. From the equation of state of a gas, Proc. R. Soc. Lond. A 106 (1924) 463–477.
[53] L.A. Viehland, A.R. Janzen, R.A. Aziz, High approximations to the transport properties of pure atomic gases, J. Chem. Phys. 102 (1995) 5444–5450.
[54] J.J. Hurly, M.R. Moldover, Ab initio values of the thermophysical properties of helium as standards, J. Res. Natl. Inst. Stand. Technol. 105 (2000) 667–688.
[55] G.C. Maitland, E.B. Smith, Critical reassessment of viscosities of 11 common gases, J. Chem. Eng. Data 17 (1972) 150–156.
[56] P.C. Jain, S.C. Saxena, Thermal conductivity of krypton in the temperature range 400–2500 K, J. Chem. Phys. 63 (1975) 5052–5053.
[57] V. Saxena, S. Saxena, Measurement of the thermal conductivity of argon using hot-wire type thermal diffusion columns, Chem. Phys. Lett. 2 (1968) 44–46.
[58] V.K. Saxena, S.C. Saxena, Measurement of the thermal conductivity of neon using hot-wire-type thermal diffusion columns, J. Chem. Phys. 48 (1968) 5662–5667.
[59] V.K. Saxena, S.C. Saxena, Thermal conductivity of krypton and xenon in the temperature range 350–1500 K, J. Chem. Phys. 51 (1969) 3361–3368.
[60] S. Weissman, Self-diffusion coefficient of neon, Phys. Fluids 16 (1973) 1425–1428.

[61] S. Weissman, G.A. DuBro, Self-diffusion coefficients for krypton, Phys. Fluids 13 (1970) 2689–2692.
[62] W. Groth, E. Sussner, Self diffusion measurements III. The self diffusion coefficient of neon, Z. Phys. Chem. (Leipz.) 193 (1944) 296–300.
[63] K. Schafer, K. Schuhmann, Zwischenmolekulare Kräfte und Temperaturabhangigkeit von Diffusion und Selbstdiffusion in Edelgasen, Z. Elektrochem. 61 (1957) 246–252.
[64] B.K. Annis, A.E. Humphreys, E.A. Mason, Nonisothermal, nonstationary diffusion, Phys. Fluids 12 (1969) 78–83.
[65] E. Winn, The temperature dependence of the self-diffusion coefficients of argon, neon, nitrogen, oxygen, carbon dioxide, and methane, Phys. Rev. 80 (1950) 1024–1027.
[66] F. Hutchinson, Self-diffusion in argon, J. Chem. Phys. 17 (1949) 1081–1086.
[67] J.H. Dymond, E.B. Smith, The Virial Coefficients of Pure Gases and Mixtures, Clarendon Press, 1980.
[68] R. DiPippo, J. Kestin, Viscosity of seven gases up to 500 °C and its statistical interpretation, in: Proceedings of the Fourth Symposium on Thermophysical Properties, College Park, MD, April 1–4, 1968, pp. 304–313.